Chemical Engineering Journal 504 (2025) 158794

Contents lists available at ScienceDirect

Chemical Engineering Journal

journal homepage: www.elsevier.com/locate/cej

A novel Solid Oxide Photoelectrolysis cell for Solar-Driven hydrogen production

Guangyu Deng, Chenyu Xu *, Jinhao Mei, Chen-Ge Chen, Yanwei Zhang *

State Key Laboratory of Clean Energy Utilization, Zhejiang University, Hangzhou 310027, PR China

ARTICLE INFO

Keywords:
solar-driven SOEC
Solid Oxide Photoelectrolysis Cell
SOEC
Hydrogen energy
Solar hydrogen production

ABSTRACT

Solid Oxide Electrolysis Cells (SOECs) hold great potential for efficient hydrogen production through water splitting. By introducing a photoresponsive electrode into an SOEC, we developed a novel Solid Oxide Photoelectrolysis Cell (SOPC) device. This device demonstrated a substantial enhancement in SOEC performance under light illumination. Various aluminum-doped lanthanum strontium titanate (ALST) photoresponsive electrode materials were synthesized using melting methods and evaluated for their photocatalytic and electrochemical performance. Notably, ALST exhibited an optimal percentage photocurrent of 21.39 % and photocurrent of 56.89 mA/cm^2, leading to a hydrogen production rate of 10.62 mol/m^2/h with an external quantum efficiency (EQE) of 30.2 %. The material also showed significant visible-light absorption at elevated temperatures, enhancing its suitability for SOPCs. This study elucidates the mechanisms by which photogenerated carriers drive photocatalysis and photoelectrochemical reactions, which are crucial for optimizing SOPC performance. Ultimately, SOPC technology provides a more efficient pathway for hydrogen production, contributing to the advancement of next-generation sustainable energy solutions.

1. Introduction

Solid Oxide Electrolysis Cells (SOECs) have emerged as a promising technology for efficient energy conversion, particularly in the context of hydrogen production via water splitting [1,2]. As the global demand for energy continues to rise and environmental concerns become more urgent, the pursuit of sustainable and efficient hydrogen production methods has gained significant attention [3,4]. Hydrogen, especially when produced from renewable energy sources, is considered a pivotal element in the transition towards a clean energy future [5]. It offers a versatile and environmentally friendly alternative to fossil fuels, with the potential to significantly reduce carbon emissions [6]. Among various hydrogen production methods, water electrolysis stands out due to its ability to integrate with renewable energy sources such as solar and wind power, facilitating the generation of "green hydrogen" [7]. SOECs are particularly advantageous for this purpose because they operate at high temperatures, which enhances the efficiency of converting electrical energy into chemical energy stored in hydrogen [8,9]. The high operating temperature not only improves the overall efficiency of the electrolysis process but also allows for the incorporation of thermal energy from renewable sources, thereby reducing the electrical energy requirement [10]. This makes SOECs an attractive option for large-scale hydrogen production, especially when integrated with renewable energy systems.

Integrating solar energy into SOECs presents a promising avenue for significantly improving the efficiency of hydrogen production [11,12]. Solar-driven SOECs harness solar energy to directly drive the water-splitting reaction, reducing the dependency on electrical energy and enhancing the overall energy conversion efficiency [13–16]. By coupling high-temperature electrolysis with concentrated solar power or other forms of solar energy, the thermal energy provided by solar radiation can be utilized to meet part of the energy demand of the electrolysis process. This integration can lower operational costs and improve the sustainability of hydrogen production. Recent advancements in solar-driven SOECs have focused on optimizing system designs [17], improving solar thermal materials [18], and exploring hybrid configurations that combine SOECs with solar thermal collectors [19] or photovoltaic systems [20]. These innovations have the potential to further enhance the efficiency of hydrogen production while reducing greenhouse gas emissions.

However, despite these advancements, a significant gap remains in the effective utilization of photogenerated carriers within SOECs, a

* Corresponding authors at: State Key Laboratory of Clean Energy Utilization, Zhejiang University, Hangzhou 310027, PR China (C. Xu).
E-mail addresses: mrxcy@zju.edu.cn (C. Xu), zhangyw@zju.edu.cn (Y. Zhang).

https://doi.org/10.1016/j.cej.2024.158794
Received 23 September 2024; Received in revised form 3 December 2024; Accepted 19 December 2024
Available online 20 December 2024

concept that is well-established in the fields of photocatalysis [21,22] and photoelectrochemistry [23,24]. In these fields, photogenerated electron-hole pairs play a critical role in driving redox reactions, allowing for the direct conversion of solar energy into chemical energy [25,26]. This principle has been successfully applied in various applications, such as pollutant degradation [27], water splitting [28], and CO_2 reduction [29]. In contrast, solar-driven SOEC systems have primarily relied on thermal energy from concentrated solar power to enhance high-temperature electrolysis, overlooking the potential benefits of integrating photogenerated carriers. The integration of photogenerated carriers into SOECs could theoretically reduce the activation energy required for electrolysis reactions, potentially lowering the operating temperature and further decreasing the electrical energy consumption. This could lead to a new generation of SOECs that are not only more efficient but also more adaptable to varying solar conditions. Nevertheless, the high operating temperatures of SOECs present challenges for the stability and efficiency of photoactive materials, which are typically optimized for lower temperature operations [30,31]. Additionally, incorporating light-absorbing materials into the SOEC architecture without compromising its structural and functional integrity poses significant engineering challenges.

$SrTiO_3$-based materials, including lanthanum strontium titanate (LST), have shown considerable potential in addressing some of these challenges. In the field of photocatalysis, $SrTiO_3$ is recognized for its strong ultraviolet (UV) light absorption and excellent stability, making it a suitable candidate for photochemical reactions like water splitting [32]. The wide bandgap and stable perovskite structure of $SrTiO_3$ enable it to generate strong oxidation potentials and high mobility of charge carriers, which are critical for enhancing photocatalytic efficiency [33,34]. Lanthanum strontium titanate (LST), a modified form of $SrTiO_3$, extends these beneficial properties into the domain of SOECs, offering improved electronic conductivity and stability at the high operating temperatures typical of SOECs [35,36]. These characteristics make LST a promising material for use as an electrode in SOECs, particularly for hydrogen production through high-temperature water splitting. Aluminum doping in $SrTiO_3$ enhances photocatalytic performance by narrowing the bandgap, improving charge separation, and increasing surface reactivity, and similar effects are expected in LST for photoelectrochemical applications [33,34].

Building on these insights, this study explores the integration of $SrTiO_3$-based materials, specifically aluminum-doped lanthanum strontium titanate (ALST), into a novel solar-driven Solid Oxide Photoelectrolysis Cell (SOPC) device. The research focuses on synthesizing and characterizing ALST materials to enhance their performance under the demanding conditions of SOPCs. By leveraging the photocatalytic properties of $SrTiO_3$ and the electrochemical performance of LST, this study aims to develop a hybrid system that effectively utilizes photogenerated carriers in a high-temperature SOEC environment. The study involves a comprehensive analysis of ALST's structural, optical, and electrochemical properties, with a focus on optimizing the material's effectiveness as a photoresponsive electrode in SOPC configurations. Experiments conducted under varying conditions, including temperature, voltage, and atmospheric composition, aim to identify the optimal parameters for maximizing hydrogen production efficiency. Additionally, the study investigates photogenerated carrier utilization mechanisms, bridging the gap between photocatalysis and SOPCs. This work not only demonstrates the feasibility of integrating photocatalysis into SOECs but also contributes to the development of advanced materials and systems for sustainable hydrogen production. By bridging the gap between photocatalysis and solid oxide electrolysis, this research paves the way for the next generation of solar-driven hydrogen production technologies, offering a more efficient and adaptable approach to meeting global energy needs.

2. Experimental

2.1. Photoresponsive electrode synthesis

The preparation of photoresponsive electrode material powder LST ($La_{0.3}Sr_{0.7}TiO_3$) was carried out using the sol–gel method [37]. A clear and transparent solution A was obtained by mixing and stirring titanium tetraisopropanolate, ethylene glycol, and citric acid (SCR, Sinopharm Chemical Reagent Co., Ltd., AR) in a molar ratio of 1:4:4. Citric acid dissolves slowly in ethylene glycol, requiring several hours for complete dissolution. A stoichiometric mixture of lanthanum nitrate hexahydrate and strontium nitrate (SCR, AR) was dissolved in water to form solution B. Solutions A and B were mixed and diluted with water to obtain a 0.5 M (final product) solution. The solution was heated and continuously stirred at 80 °C until it transitioned sequentially from a colorless solution to a yellow sol and then to a brown gel. The resulting gel was heat-treated in an oven at 200 °C for 12 h, followed by ball milling for 2 h to obtain the powder. The powder was then heat-treated at 550 °C for 5 h, followed by ball milling for 2 h, and further heat-treated at 800 °C for 5 h, followed by ball milling for 2 h. After each milling process, the powder was sieved through a 400 mesh screen.

The preparation of photoresponsive electrode material powders 4ALST (0.04Al-$La_{0.3}Sr_{0.7}TiO_3$) and 8ALST (0.08Al-$La_{0.3}Sr_{0.7}TiO_3$) were carried out using the melting method, with the aforementioned LST as the precursor [38]. Stoichiometric amounts of nano-alumina (Macklin, 99.99 %) and LST powder were mixed and ball-milled for 2 h. Strontium chloride (SCR, AR) was added to achieve a final product-to-strontium chloride molar ratio of 1:10. The mixture was placed in a corundum crucible and heated at a rate of 2 °C/min to 1150 °C in an air atmosphere, where it was held for 10 h. The product was thoroughly mixed with water and centrifuged (it is recommended to use a centrifuge speed $>$ 10,000 rpm for complete separation) several times (for reference, the material was centrifuged 20 times) until the pH of the centrifuged liquid was 7. The solid product was dried and ball-milled for 2 h to obtain the powder.

2.2. Cell preparation

The construction of the 8ALST/YSZ($(Y_2O_3)_{0.08}(ZrO_2)_{0.92}$)/YSZ-LSM (YSZ-$(La_{0.75}Sr_{0.25})_{0.95}MnO_3$) full cell, involved the possibility of substituting the 8ALST with any of the photoresponsive electrodes discussed in this paper, as shown in Fig. S23 [39]. The cell adopts an electrolyte-supported structure, utilizing commercial YSZ (Suzhou Huaqing) in the form of a 35 mm square with a thickness of 0.2 mm. The cathode powder materials, comprising commercial YSZ and LSM (Sofcman), were mechanically mixed in a mass ratio of 1:1 and ball-milled for 2 h to produce YSZ-LSM. The powder was then sieved through a 400 mesh screen. A mixture of 7.5 wt% ethyl cellulose in terpineol and the powders was prepared in a 1:1 mass ratio to create the photoresponsive electrode 8ALST ink and YSZ-LSM ink, respectively. The preparation of the inks requires thorough mixing of the powders with the solvent to prevent uneven printing or clogging. As a reference, a pestle was used in a mortar to stir the mixture in one direction (e.g., clockwise) for 1 h. The ink required for each printing was approximately 0.5 g. The YSZ-LSM ink was screen-printed onto the center of one side of the YSZ, forming a 5 cm^2 circular pattern. The photoresponsive electrode 8ALST ink was screen-printed onto the center of the other side of the YSZ, forming a 1 cm^2 circular pattern. A 250 mesh polyester screen was used for the ink screen printing. The cell underwent heat treatment at 1200 °C for 2 h, with a temperature change rate of 0.5 °C/min above 800 °C and 1 °C/min below 800 °C.

A grid-patterned silver current collector was employed to ensure conductivity and direct light exposure to the photoresponsive electrode. This grid consisted of equally spaced horizontal and vertical lines with an interline spacing of approximately 2.8 mm, covering about one-third of the surface area. The silver current collectors, matching the size of the

electrodes, were screen-printed using silver paste (DAD-87) ink. A 100 mesh polyester screen was used for the silver current collector screen printing. Silver wires (Ag 99.99 %) were attached to form a four-electrode structure. A high-temperature adhesive (Aremco Ceramabond 552) was used to bond corundum weight rings to the backlight side of the cell.

2.3. Solid oxide photoelectrolysis cell (SOPC) test

The SOPC experimental system (Fig. S1) used in this study has been detailed in previous work and is employed to achieve light conduction while maintaining stable cell temperature [40]. The cell's photoresponsive electrode faces the quartz light guide column, with high borosilicate glass used for high-temperature sealing. The electric furnace was heated to 850 °C and maintained for 5 h, then lowered to the experimental temperature (typically 800 °C, with a range of 600–850 °C) at a rate of 1 °C/min. The anode carrier gas was 100 sccm of argon, while the cathode carrier gas was a mixture of water vapor, hydrogen, and argon, maintaining a total flow rate of 100 sccm (typically 50 % H_2O + 50 % Ar). The water vapor was quantitatively controlled by a syringe pump, and the other gases were measured using flow meters (Alicat). The light source was a 300 W xenon lamp (Perfectlight), providing a light intensity of 0.4 W/cm^2 on the photoresponsive electrode. The power supply was an electrochemical workstation (Ivium). Gas products were detected using a gas chromatograph (Agilent 7820A).

The main experiment involved alternating light and dark conditions, with cycles of 1 h of dark and 1 h of light under constant voltage (0.8–2 V). Linear sweep voltammetry (LSV) tests were conducted from −0.8 V to −2 V, with a scan rate of 0.3333 mV/s. For LSV tests involving alternating light and dark conditions, the duration of light or dark periods was 5 min at 0.1 V intervals. In cyclic voltammetry tests, the potential range was −0.8 to −2.0 to −0.8 V, with a scan rate of 50 mV/s, repeated for 100 cycles. Electrochemical impedance spectroscopy (EIS) tests were performed under constant voltage (0.8–2 V) with a frequency range of 100 kHz to 0.1 Hz, 10 points per decade, and an amplitude of 50 mV. Incident photon-to-current efficiency (IPCE) tests were conducted in situ within the SOPC experimental system under constant voltage conditions (typically 2.0 V), using the main xenon lamp light source with bandpass filters (Perfectlight). The duration of light or dark periods was 5 min.

2.4. Characterization

The Electron Paramagnetic Resonance (EPR) results were obtained using a Bruker EMX PLUS instrument at 100 K with samples loaded in quartz capillaries. The Photoluminescence (PL) measurements were conducted using an Edinburgh FLS1000 instrument, with the steady-state PL light source at 255 nm and the transient PL light source at 375 nm. Brunauer-Emmett-Teller (BET) results were acquired using a Micromeritics ASAP 2460. High-Resolution Transmission Electron Microscopy (HR-TEM) and corresponding Energy Dispersive Spectroscopy (EDS) mapping images were obtained using an FEI Talos F200X G2. X-Ray Diffraction (XRD) results were recorded using a Panalytical X'Pert3 Powder instrument equipped with a Cu Kα irradiation source. X-ray Photoelectron Spectroscopy (XPS) results were obtained using a Thermo Scientific K-Alpha instrument equipped with an Al Kα irradiation source and calibrated with adventitious carbon at a binding energy of 284.8 eV. Inductively Coupled Plasma Optical Emission Spectrometry/Mass Spectrometry (ICP-OES/MS) results were acquired using an Agilent 5110 (OES). Both conventional and in-situ (variable temperature) Ultraviolet–Visible (UV–Vis) absorption spectra were recorded using a Shimadzu UV-3600i Plus. The Mott-Schottky plots were characterized using a three-electrode system at room temperature, with a glassy carbon working electrode, a platinum counter electrode, and a saturated Ag/AgCl reference electrode in an electrolyte of 0.5 M Na_2SO_4 + 0.1 M $NaHCO_3$ (pH = 8.0). The in-situ Fourier Transform Infrared (FTIR) spectra were obtained using Bruker INVENIO-S, to prevent interference, we blocked the xenon lamp during 30 s FTIR scans every 5 min.

3. Results and discussion

3.1. Crystal structure and morphology

The Inductively Coupled Plasma (ICP) analysis revealed actual aluminum doping levels of 4.43 mol% and 8.32 mol% for 4ALST and 8ALST, respectively, which align with the initial raw material concentrations. This confirms the successful aluminum doping via the melting method, with slightly higher values attributed to the aluminum content of the corundum crucible used in the process. The X-Ray Diffraction (XRD) results (Fig. S2) show that all three materials have a cubic perovskite structure, with the (110) plane as the main peak [41]. The main peaks of LST, 4ALST, and 8ALST shift sequentially to higher angles. This shift is attributed to the substitutional doping of aluminum, which has a smaller atomic radius, causing a reduction in lattice parameters.

The Transmission Electron Microscopy (TEM) images (Fig. S3) visually demonstrate the morphological changes of the materials. The cluster diameters of all three materials are approximately 100 nm. LST exhibits multiple irregular, nearly spherical clusters, resulting in a high specific surface area. In contrast, 4ALST forms a single entity between a cube and a sphere, while 8ALST consists of highly regular cubic shapes. The evolution from LST to 4ALST to 8ALST is accompanied by a decrease in specific surface area and an increase in morphological regularity. On one hand, the reduction in specific surface area may hinder electrochemical reactions, potentially contributing to poorer electrical performance. On the other hand, the regular morphology might enhance carrier transport and reduce recombination, thereby improving photo performance. Additionally, the lattice fringes in the TEM images indicate lattice spacings of 0.277, 0.276, and 0.275 nm for LST, 4ALST, and 8ALST, respectively, all corresponding to the (1 1 0) plane of the perovskite structure based on LST [41]. High-Angle Annular Dark Field (HAADF) images (Fig. S4) reveal the uniform distribution of elements within the 8ALST cubic structure. Scanning Electron Microscopy (SEM) images (Fig. S5) display similar morphological features and evolution as seen in TEM.

The Ultraviolet–Visible (UV–Vis) spectra of LST, 4ALST, and 8ALST (Fig. S7a) show that they are typical ultraviolet-absorbing semiconductors at room temperature. The band gaps of LST, 4ALST, and 8ALST, obtained using the Tauc plot method (Fig. S7b), are 3.16 eV, 3.20 eV, and 3.21 eV, respectively, indicating that aluminum doping slightly widens the band gap [42]. The flat band potentials (considered as conduction band potentials) for LST, 4ALST, and 8ALST, derived from the Mott-Schottky (MS) plot (Fig. S6), are −1.38 V, −1.87 V, and −1.49 V vs. Ag/AgCl, respectively [43]. Therefore, the band structures of the materials, shown in Fig. S7c, suggest that all tested materials are capable of photocatalytic overall water splitting.

The Scanning Electron Microscopy (SEM) cross-sectional images of the cell (Fig. S8) clearly show the three-layer electrolyte-supported cell structure.

3.2. Light contribution in current of SOPC

Photoresponsive electrode/YSZ/YSZ-LSM cells with three different photoresponsive electrodes (8ALST, 4ALST, and LST) were subjected to constant voltage alternating light–dark experiments on the cathode side under an atmosphere of 20 % H_2O (and 80 % Ar, unspecified percentage atmosphere is Ar in this work), as shown in Fig. 1a. In this study, the percentage photocurrent (ΔC/Cdark) is used as the primary quantitative metric, as shown in Fig. S9(c, f, i). On one hand, the relative photocurrent allows us to focus on optical properties without the influence of electrical performance, which has been extensively studied in

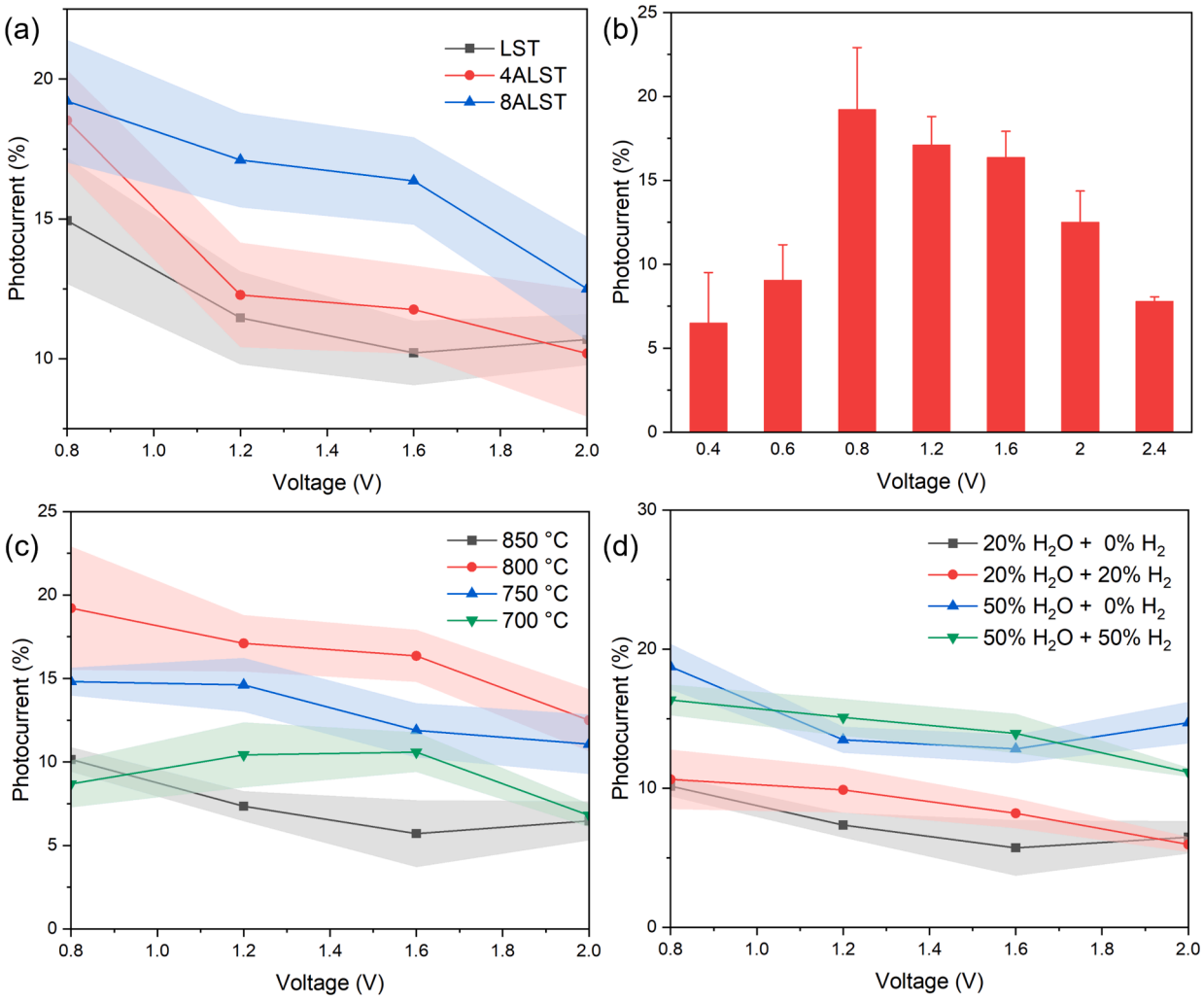

Fig. 1. Percentage photocurrents from the alternating light–dark experiments conducted at constant voltage for the photoresponsive electrode/YSZ/YSZ-LSM cell, unspecified percentage atmosphere is Ar in this work. (a) LST, 4ALST, and 8ALST photoresponsive electrodes at 800 °C and 20 % H_2O; (b) Voltage variation from 0.4 to 2.4 V for 8ALST at 800 °C and 20 % H_2O; (c) Temperature variation from 700 to 850 °C for 8ALST at 20 % H_2O; (d) Atmosphere variation from 0 to 50 % H_2 and 20 to 50 % H_2O for 8ALST at 850 °C.

traditional Solid Oxide Electrolysis Cells (SOECs) and is not the focus of this work. On the other hand, SOPC aims to replace part of the electrical energy with solar energy to achieve photo-thermo-electrochemical hydrogen production at low voltages, making the percentage photocurrent metric more relevant to this goal.

For LST and 4ALST, the maximum percentage photocurrent is achieved at 0.8 V and decreases with increasing voltage, indicating poor performance at high voltages. This could be attributed to insufficient photoactive sites on LST and 4ALST under the high hydrogen production rates associated with higher voltages [44]. In contrast, for 8ALST, the percentage photocurrent remains above 15 % in the 0.8–1.6 V range, demonstrating stability across various conditions. The highest percentage photocurrent 19.21 % is observed for 8ALST at 0.8 V. Furthermore, 8ALST shows significantly better percentage photocurrent than LST and 4ALST in the mid-voltage range of 1.2–1.6 V. Overall, the 8ALST photoresponsive electrode exhibits superior optical performance under all conditions, making it the primary material for further experiments and discussions.

Specifically, Fig. S9(a, d, g) illustrates the changes in the absolute value of the current. Significant differences in current between light (yellow) and dark (gray) conditions were observed for all three photoresponsive electrodes, indicating substantial photocurrent. This is likely due to the excellent photo properties of the B-site Ti in the perovskite structure (referencing $SrTiO_3$) [45]. In the voltage sequence of 0.8, 1.2, 1.6, and 2.0 V, the photocurrent positively correlated with increasing voltage, and the absolute value of the photocurrent was significant only at the high voltage of 2.0 V while negligible at 0.8 V, indicating that the system is primarily driven by electrolysis with light acting as an auxiliary factor. Additionally, the rate of change of current over time (dC/dt) may also differ between light and dark conditions, significantly affecting the cell's degradation behavior. This is known as the light healing effect, which has been discussed in detail in previous work; this study focuses mainly on the change in current (ΔC). At 2.0 V, the dark current values for 8ALST, 4ALST, and LST were 134.8, 140.5, and 220.6 mA/cm^2, respectively, indicating that the Al doping of photoresponsive electrodes via the melting method reduced the cell's electrical performance.

Experiments were conducted over a broader voltage range (0.4–2.4 V) beyond the typical operating voltages of SOEC (0.8–2.0 V). Fig. 1b shows the percentage photocurrent at low voltages (0.4, 0.6, 0.8 V), where the percentage photocurrent decreases sequentially with decreasing voltage. At higher voltages (0.8–2.4 V), the percentage photocurrent increases with decreasing voltage, but this trend reverses at low voltages, with the percentage photocurrent peaking at 0.8 V. This suggests that the SOPC experimental system's optical performance is optimal at the lower voltage limit of the water-splitting reaction. Additionally, there is a hypothesis that light can independently provide

energy, exhibiting excellent hydrogen evolution activity at ultra-low voltages, similar to photocatalysis, resulting in abnormally high percentage photocurrents. However, the lower percentage photocurrents at low voltages essentially refute this hypothesis, further confirming the auxiliary role of light. Under the current system, it is insufficient to achieve excess production below the water-splitting voltage through independent light energy input.

Fig. 1c shows the results of the temperature variation experiments (700, 750, 800, 850 °C). For the percentage photocurrent, the trend caused by temperature changes is consistent across all tested voltages, with the lowest percentage photocurrent observed at 850 °C, followed by 750 °C, and the highest at 800 °C. The percentage photocurrent remains relatively stable when varying the voltage at all tested temperatures, with the relative difference (ΔPPC/PPC) at high and low voltages being less than or equal to 36.2 %. The percentage photocurrent gradually decreases with increasing voltage. The differences in percentage photocurrent between different temperatures are substantial, especially between 850 °C and 800 °C, where the relative difference (ΔPPC/PPC) reaches up to 186.6 % (5.709 % to 16.36 % of percentage photocurrent). Since the percentage photocurrent is relatively stable and less influenced by electrical performance, the significant difference between 850 °C and 800 °C indicates a major discrepancy in the material's optical properties at different temperatures, further explaining the peak absolute photocurrent at 800 °C. Over the temperature range of 750 °C to 850 °C, the material's optical performance initially improves and then degrades due to the interplay of temperature-dependent factors. From 750 °C to 800 °C, the moderate enhancement in optical performance is attributed to improved photocatalytic and photoreaction kinetics at elevated temperatures [46], which enhance charge carrier mobility and separation. Although oxygen vacancy content increases slightly, it remains below a threshold where recombination losses are significant. However, from 800 °C to 850 °C, a substantial increase in oxygen vacancy content occurs [47,48], creating numerous recombination traps that lead to severe recombination of photogenerated carriers [49]. Additionally, the intrinsic shortening of carrier mean free path due to increased phonon interactions at higher temperatures [50] exacerbates recombination losses. These detrimental effects overshadow the benefits of elevated temperature, resulting in a net degradation of optical performance. Therefore, the system achieves optimal comprehensive performance at 800 °C. The results at 700 °C align with the behavior observed in 750–850 °C, giving further support.

The results of the atmosphere variation experiments are shown in Fig. 1d. The atmospheric conditions include four scenarios: 20 %-50 % water content, both with and without hydrogen. The percentage photocurrent under different atmospheric conditions shows distinct and interesting results. The percentage photocurrent is divided into two groups based on the water content: 20 % water and 50 % water. The percentage photocurrent for the 50 % water group is significantly higher than for the 20 % water group, while the presence or absence of hydrogen has little effect. This trend is opposite to that of the absolute photocurrent (Fig. S14b). In multiphase photocatalysis, the water vapor content is known to significantly affect the hydrogen production of the material [51], which might explain the impact of water content on optical performance and, consequently, on the percentage photocurrent observed in this study. Between the 50 % H_2O + 0 % H_2 atmosphere and the 50 % H_2O + 50 % H_2 atmosphere, the former shows a higher average percentage photocurrent, with the percentage photocurrent still exceeding 15 % at 2.0 V. Therefore, the 50 % H_2O + 0 % H_2 atmosphere is considered the typical condition for further discussion.

Additionally, the absolute photocurrent results for temperature and atmosphere variations (Fig. S14) were also discussed. For the absolute photocurrent in response to temperature variation (Fig. S14a), the trend was consistent across all tested voltages, with the lowest photocurrent observed at 700 °C, followed by 750 °C, 850 °C, and the highest at 800 °C. The photocurrent's sensitivity to temperature changes is notable; a 50 °C increase results in a 105.5 % difference in photocurrent (from 8.182 mA/cm2 at 750 °C to 16.81 mA/cm2 at 800 °C). The photocurrent peaks at 800 °C, displaying a parabolic relationship with temperature, contrasting with the simple positive correlation between current and temperature typically observed in conventional SOECs. The lower photocurrent at 850 °C may indicate significant degradation of the material's optical performance at elevated temperatures.

The absolute photocurrent of the atmosphere variation experiments are shown in Fig. S14b. The absolute photocurrent results reveal two distinct groups: one with hydrogen and one without. The presence or absence of hydrogen causes a significant difference in photocurrent, while variations in water content have little impact on photocurrent. This suggests that the results are a byproduct of changes in electrochemical performance. In traditional SOECs, a hydrogen atmosphere significantly increases the oxygen vacancy and Ti^{3+} content in the cathode material, greatly enhancing electrical performance [35,52,53]. Furthermore, a 20 % water content may be sufficient for electrolysis, rendering the system insensitive to higher water content. An exception to the trend is observed at 2.0 V and 50 % H_2O + 50 % H_2, where the maximum photocurrent of 56.89 mA/cm^2 is achieved, corresponding to a hydrogen production rate of 10.62 mol/m^2/h. Under a xenon lamp light intensity of 0.4 W/cm^2, the external quantum efficiency (EQE) is 30.2 %. Since the percentage photocurrent at this point remains within the typical range of 10–20 %, the enhancement can be attributed to improved electrical performance. Additionally, the conditions of high temperature, high voltage, and high atmosphere coincide with the peak points of both current and photocurrent, indicating that the maximum current and maximum photocurrent occur under the same conditions.

3.3. Light effects in SOPC experiments

Further SOPC experiments of the 8ALST photoresponsive electrode at 800 °C and 50 % H_2O + 0 % H_2 atmosphere were conducted. The absolute photocurrent (Fig. S15a) reaches a maximum value of 25.43 mA/cm^2 at 2.0 V. Beyond the photocurrent itself, the significant difference in slope between the dark and light conditions suggests the presence of a sustained photo-response (i.e., Light Healing Effect, LHE), which influences cell degradation over a longer time scale. The percentage photocurrent (Fig. S15b) peaks at 21.39 % at 0.8 V. The central temperature of the illuminated surface of the cell (i.e., the photoresponsive electrode) is shown in Fig. S15c. Unlike the significant changes in photocurrent, the cell temperature remains stable throughout the in-situ experiment. The average temperature during dark conditions is 799.6 °C, and 800.8 °C during light conditions, with a light–dark temperature difference of only 1.2 °C. Such a small temperature difference is insufficient to cause significant current variations, indicating that the photocurrent observed in this study is not due to a photo-thermal pathway. The photo-thermal effect is negligible in this study due to the low light intensity (0.4 W/cm^2) and the small temperature difference. According to existing optical theory, it is highly likely that the photocurrent is due to photocatalytic or photoelectrochemical mechanisms [54,55]. Besides, the results of full-covered cell without direct illumination of the photoresponsive electrode (Fig. S15d), showed a 1.48 % current increase, indicating the primary effect is not photothermal. The lower unit area performance of SOPC compared to full-covered cell, is due to current collectors covering only one-third of the electrode, which can be optimized with patterned design.

Gas product testing was conducted, with the results shown in Fig. S16. In the Faraday efficiency test, there was good consistency between the current and hydrogen production rate over the entire time period. The average current was 188.8 mA/cm^2, and the average hydrogen production rate was 34.66 mol/m^2/h, resulting in a Faraday efficiency of 98.35 %. Qualitatively, the current and hydrogen production are considered to have a one-to-one correspondence, indicating that electronic current and side reactions are negligible. Comparing the hydrogen and oxygen production rates, the hydrogen to oxygen ratio was 2.049, indicating complete water splitting.

Fig. 2a shows the results of the constant current test, conducted at 100 mA/cm^2 with 5-minute light–dark intervals. The average voltage in the dark was 1.858 V, while the average voltage under illumination was 1.814 V. Illumination caused a voltage drop of 0.045 V, indicating that 2.46 % of the electrical energy was replaced by solar energy. Notably, this energy replacement is attributed to the photocatalytic/photoelectrochemical pathway, with potential for additional photo-thermal energy contribution (from over 1.5 V in conventional SOECs to less than 1.0 V in solar-driven SOECs, suggesting at least a 33.3 % energy contribution). Furthermore, this study employed low light intensity, leaving room for a higher proportion of electrical energy replacement.

Fig. 2b presents the results of the 40-hour steady-state light–dark test at a constant voltage of 1.6 V. The cell experienced performance degradation under both light and dark conditions over 40 h, with the changes appearing linear (dC/dt = constant). In the dark, the current decreased from 52.78 mA/cm^2 to 40.35 mA/cm^2, with a rate of approximately −6.67 ‰/h. Under illumination, the current decreased from 55.49 mA/cm^2 to 51.51 mA/cm^2, with a rate of about −1.86 ‰/h. Illumination significantly mitigated the cell's degradation rate, reducing it to 27.9 % of the rate in the dark and extending the cell's lifespan to 3.59 times that under dark conditions. This deceleration of cell degradation under illumination is likely due to light-induced alleviation or even reversal of oxygen vacancy formation [40], which mitigates interface oxygen accumulation and secondary phase formation (the primary degradation mechanisms in SOECs) [56,57]. This phenomenon is referred to as the Light Healing Effect (LHE).

Fig. S17 shows the Linear Sweep Voltammetry (LSV) results under steady-state light, steady-state dark, and alternating light–dark conditions. The standard deviation across multiple tests (shaded area) is less than 5 % for both steady-state light and dark conditions, demonstrating good consistency and reproducibility. The current range during alternating light–dark conditions falls mostly between the steady-state light and dark values, with a high degree of overlap between alternating and steady-state conditions, indicating system stability under alternating illumination. With a 5-minute light–dark interval, the results of the alternating experiments cover most of the range between the steady-state light and dark conditions, suggesting that the majority of the photocatalytic/photoelectrochemical response time is less than 5 min, though some light responses may last longer than 5 min. Additionally, at low voltages, the alternating condition closely resembles the dark steady-state, while at high voltages, it approaches the light steady-state. Given that LSV is a forward scan, it can be inferred that the cell initially resembles the dark steady-state and, through changes induced by the photo-response during alternating illumination, gradually approaches the light steady-state.

Further Incident Photon-to-Current Efficiency (IPCE) tests using bandpass filters in the 350–800 nm range demonstrated the monochromatic light response characteristics. As shown in Fig. S18a, at 800 °C, 2.0 V, and 50 % H_2O + 0 % H_2, the IPCE curve displayed a nearly linear decrease with increasing wavelength from 350-800 nm, with the IPCE reaching 19.3 % at 350 nm and still at 5.4 % at 800 nm. Comparing the relative IPCE values at different temperatures (Fig. 2c), it is evident that visible-light absorption decreases sequentially at 800 °C, 700 °C, and 600 °C, exhibiting nearly exponential decay rather than linear at

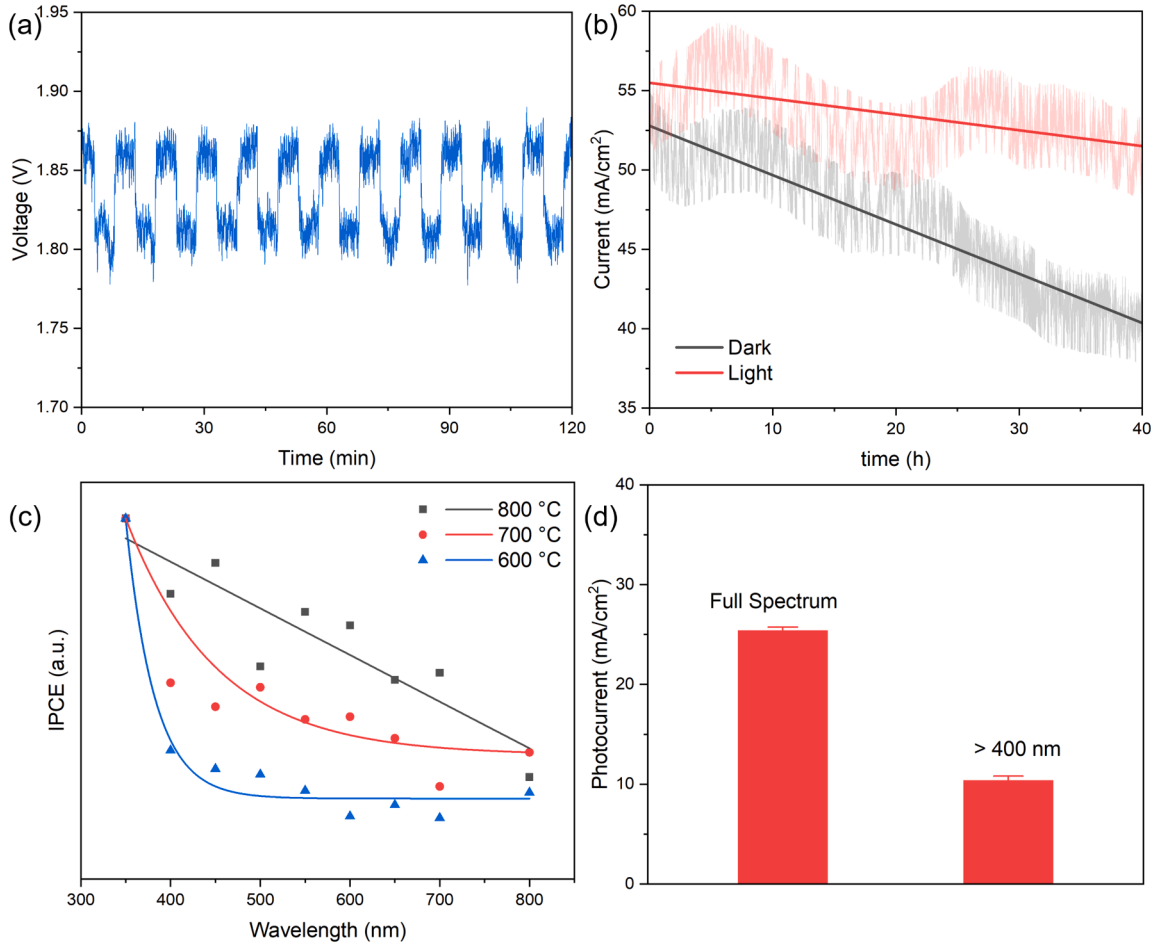

Fig. 2. Advanced SOPC tests of the 8ALST photoresponsive electrode at 800 °C and 50 % H_2O. (a) Constant current test at 100 mA/cm^2 with 5-minute light–dark intervals; (b) 40-hour steady-state light–dark test at 1.6 V; (c) SOPC Incident Photon-to-Current Efficiency (IPCE) test from 600 to 800 °C at 2.0 V; (d) Variable wavelength experiment for the full spectrum and visible light (>400 nm) at 2.0 V.

lower temperatures, indicating less pronounced visible-light absorption. However, as shown in Fig. S18, the relative spectral response within 350–800 nm remains largely unchanged (maintaining a near-linear characteristic) in the IPCE trend under varying atmospheres (50 % H_2O + 50 % H_2) and voltages (0.8 V). In summary, while 8ALST is a semiconductor that primarily absorbs ultraviolet light at room temperature, it demonstrates significant visible-light absorption at 800 °C. The relative spectral response characteristics are greatly influenced by temperature but are relatively unaffected by voltage and atmosphere. The variable wavelength experiment (Fig. 2d, Fig. S19) confirmed this hypothesis, showing that in SOPC experiments, 8ALST exhibited significant photocurrent under > 400 nm light, even in the absence of ultraviolet light.

3.4. Optical properties

The steady-state Photoluminescence (PL) results (Fig. 3a) show a main peak at 396.2 nm and a secondary peak at 544.4 nm, with the latter corresponding to impurity levels caused by oxygen vacancies [58]. The main peak intensity significantly decreases from LST to 4ALST, indicating that aluminum doping reduces radiative recombination, thereby enhancing the material's photo performance. However, the difference in the main peak intensity between 4ALST and 8ALST is negligible, suggesting that aluminum content beyond 4 % does not further reduce the recombination rate of photogenerated carriers. For the secondary impurity level peak, the intensity increases with aluminum doping, indicating more oxygen vacancies and stronger impurity recombination. The increase in oxygen vacancies due to aluminum doping might be a double-edged sword: while it acts as a recombination trap, it also enhances carrier transport [34]. The Time-Resolved Photoluminescence (TRPL) results (Fig. 4c) are also consistent with these findings, showing fluorescence lifetimes of 0.272 ns for LST, 0.301 ns for 4ALST, and 0.293 ns for 8ALST. The increased carrier lifetime from LST to 4ALST is due to a lower recombination rate, while the decreased lifetime from 4ALST to 8ALST is due to intensified impurity recombination and enhanced carrier transport.

The Brunauer-Emmett-Teller (BET) results (Fig. S20a) display the water adsorption characteristics of each material, with the water adsorption volumes for LST, 4ALST, and 8ALST being 15.81, 8.468, and 7.610 cm^3/g STP, respectively. LST has a significantly higher water adsorption volume than 4ALST, while 4ALST and 8ALST have similar values, with 8ALST being slightly lower. This difference is likely due to the reduced specific surface area caused by the melting method.

The Electron Paramagnetic Resonance (EPR) results (Fig. S20b) show that the g = 2.003 signal corresponds to oxygen vacancies, and the peak area represents the relative bulk oxygen vacancy content [59]. The peak area ratios for LST, 4ALST, and 8ALST are 1:2.66:3.87, indicating that aluminum doping significantly increases the bulk oxygen vacancies in LST, with the oxygen vacancy content positively correlated with the aluminum doping level.

The X-ray Photoelectron Spectroscopy (XPS) results (Fig. S20c) show the deconvolution of the O1s orbital peaks at 529.5, 530.9, and 531.7 eV, corresponding to lattice oxygen (OL), oxygen vacancies (OV), and chemisorbed oxygen (OC), respectively, quantified by peak area [60]. From LST to 4ALST, the main change is the increase in the OC ratio from 12.4 % to 17.8 %. A higher OC ratio indicates improved water adsorption capacity, suggesting that aluminum doping via the melting method enhances water adsorption properties, which may contribute to the

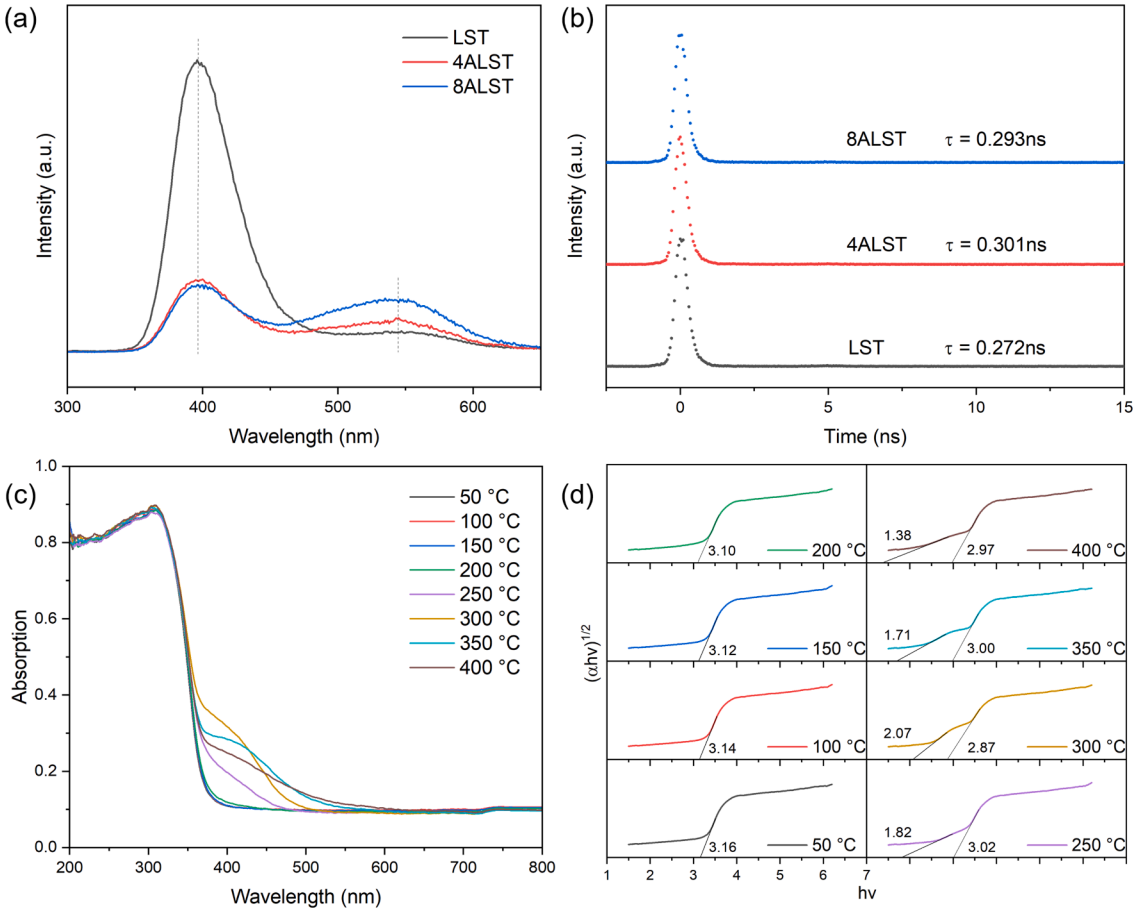

Fig. 3. (a) Steady-state Photoluminescence (PL) and (b) Time-Resolved Photoluminescence (TRPL) material characterizations of LST, 4ALST, and 8ALST. (b) Variable temperature UV–Vis spectra and (c) Tauc plot from 50-400 °C of 8ALST.

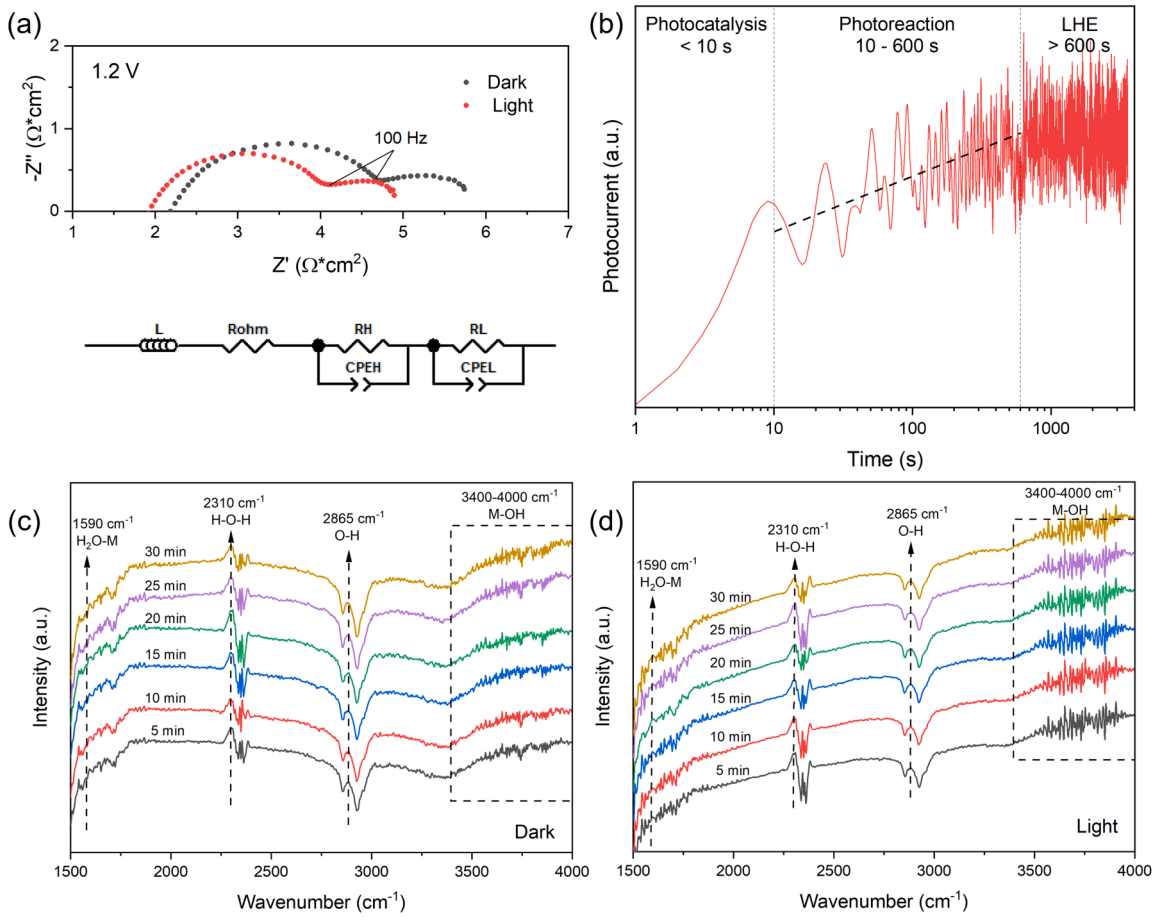

Fig. 4. SOPC characterizations of the 8ALST photoresponsive electrode at 800 °C and 50 % H_2O: (a) Electrochemical Impedance Spectroscopy (EIS) under light and dark conditions; (b) Time-frequency analysis of light response. In-situ Fourier Transform Infrared (FTIR) spectra at (c) dark and (d) light conditions at 500 °C.

improved photo performance. From 4ALST to 8ALST, the OV ratio decreases from 10.4 % to 5.8 %. Given that XPS typically probes a depth of 1–10 nm, reflecting surface properties, the lower OV ratio might result from easier oxygen incorporation from the air and water adsorption [61]. Higher adsorption and reaction activity could facilitate carrier transport, partially explaining the PL results. The differences between EPR and XPS results regarding oxygen vacancies arise from their differing characterization depths.

Additionally, the XPS results (Fig. S20d) show the deconvolution of the Ti2p orbital peaks, with peaks at 457.4 and 463.1 eV corresponding to Ti^{3+}, and peaks at 458.4 and 464.2 eV corresponding to Ti^{4+}, quantified by peak area; the lower binding energy peaks correspond to the Ti2p 3/2 orbital, and the higher binding energy peaks correspond to the Ti2p 1/2 orbital [60]. The Ti^{3+} ratios for LST, 4ALST, and 8ALST are 18.9 %, 9.7 %, and 8.2 %, respectively. A significant decrease in Ti^{3+} content is observed from LST to 4ALST, with only a slight decrease from 4ALST to 8ALST. In the context of SOECs, Ti^{3+} is highly correlated with oxygen transport and electrocatalytic performance; thus, the decrease in Ti^{3+} content could explain the sequential reduction in current observed in the main experiments for LST, 4ALST, and 8ALST [35]. In photocatalysis, Ti^{3+} is considered a recombination center for $SrTiO_3$-based materials; therefore, the reduction in Ti^{3+} leads to decreased carrier recombination and enhanced optical performance [34]. This explanation aligns with the main experimental results and PL data. In summary, the adjustment of Ti^{3+} content represents a trade-off between photo performance and electrical performance, indicating that it is a key factor in the modification of Ti-based SOPC materials.

The variable temperature UV–Vis spectra of 8ALST are shown in Fig. 3c. Between 50–200 °C, the material continues to behave as an ultraviolet-absorbing semiconductor. However, between 250–400 °C, a significant broad absorption band in the visible light range appears, which visually redshifts with increasing temperature [42]. This high-temperature visible-light absorption is likely due to the increase in oxygen vacancies in the material. The Tauc plots (Fig. 3d) quantitatively characterize the changes in band gap with temperature. The band gaps of 8ALST at 50, 100, 150, and 200 °C are 3.16 eV, 3.14 eV, 3.12 eV, and 3.10 eV, respectively, showing a linear and slight reduction in the band gap with increasing temperature, consistent with the temperature-dependent optical characteristics of stable semiconductors. Between 250–400 °C, the presence of non-negligible intraband gap absorption affects the band gap, making accurate quantitative results from the Tauc plot method unattainable, although qualitative analysis is still possible. Anomalously strong interactions between intraband gap states and the band gap are observed at 300 °C, though the cause remains unclear. Overall, from 250-400 °C, the band gap narrows slightly with increasing temperature, while the intraband gap shrinks significantly. This narrow intraband gap and visible-light absorption at high temperatures may contribute to the visible light response of 8ALST in SOPC applications.

3.5. Interface reactions

The Electrochemical Impedance Spectroscopy (EIS) results under dark and light conditions (Fig. 4a) show a reduction in the overall cell impedance when illuminated, with the spectrum divided into high-frequency and low-frequency processes at 100 Hz. The cell impedance was modeled using a dual-process equivalent circuit with inductive correction, decomposed into ohmic impedance (R_{ohm}), high-frequency impedance (R_H), and low-frequency impedance (R_L) [62,63]. Under

dark conditions, R_{ohm}, R_H, and R_L are 1.986, 2.968, and 0.961 Ω*cm^2, respectively. Under light conditions, these values decrease to 1.748, 2.451, and 0.904 Ω*cm^2, respectively. Illumination causes a significant reduction in R_H and a slight decrease in both R_{ohm} and R_L, with the reduction in R_H accounting for 63.7 % of the total impedance decrease. R_{ohm} corresponds to the electrolyte's ohmic resistance and is highly related to bulk oxygen vacancies [64]. R_H, occurring in the frequency range of 10^2-10^5 Hz, corresponds to charge transfer resistance and is closely associated with carriers [65]. R_L, in the frequency range of 10^{-1}-10^2 Hz, corresponds to the impedance related to water diffusion and adsorption, and is influenced by electrode oxygen vacancies and structural factors [65]. It can be inferred that the reduction in R_H is due to the photogenerated carriers enhancing the charge transfer process of the hydrogen evolution reaction (HER), indicating that the photocatalytic mechanism primarily drives the reduction in R_H and the generation of photocurrent. Additionally, the slight decreases in R_{ohm} and R_L are attributed to the photoreaction, which increases oxygen vacancies on the photoresponsive electrode surface and throughout the cell, contributing partially to the photocurrent. The EIS results within the 0.8–2.0 V range (Fig. S21) are more complex. Qualitatively, the high-frequency impedance accounts for a larger proportion of the total impedance at lower voltages than at higher voltages, suggesting that lower voltages favor the reduction of high-frequency impedance dominated by photocatalysis. This provides a strong explanation for the preference for lower voltages in achieving higher percentage photocurrents.

Furthermore, the time–frequency analysis of the light response (Fig. 4b) more clearly illustrates the cell's photo-response behavior across different time scales. Based on the slope differences (d(PC)/d(log (t))), the photo-response behavior can be qualitatively divided into three stages: less than 10 s, between 10–600 s, and greater than 600 s. The rapid photo-response within less than 10 s is attributed to photogenerated carriers facilitating easier overcoming of the reaction energy barrier for the hydrogen evolution reaction (HER), which follows the photocatalytic pathway. The medium-speed photo-response between 10–600 s is due to photogenerated carriers causing reactions in the photoelectrode material, leading to an increase in oxygen vacancies at the cathode and, subsequently, in the entire cell, following the photoelectrochemical pathway. This further explains and confirms the reduction in ohmic and low-frequency impedance observed in the Electrochemical Impedance Spectroscopy (EIS) results under illumination. The slow photo-response greater than 600 s is attributed to the Light Healing Effect (LHE), which manifests significant differences only in long-term steady-state tests (as shown in Fig. 2b).

The in-situ Fourier Transform Infrared (FTIR) spectra reveal the changes in surface groups during the reaction process. The peaks at 1590, 2310, 2865, and 3400–4000 cm^{-1} correspond to the vibrations of H_2O-M, H-O-H, O-H, and M−OH (where M denotes metal Ti, Sr, La, or Al) groups, respectively [66,67]. During the temperature increase from 50-500 °C (Fig. S22), the H_2O-M peak first strengthens and then weakens. The initial strengthening is likely due to the kinetic advantage of water adsorption at high temperatures, while the subsequent weakening may result from the thermodynamic difficulty of water adsorption at even higher temperatures (i.e., higher energy barriers for water adsorption at elevated temperatures). The H-O-H group gradually strengthens, indicating enhanced vibration of water molecules at higher temperatures. Hydroxyl-related groups only show increased intensity below 300 °C and remain relatively unchanged at higher temperatures. Since hydroxyl groups correspond to intermediate species in the water splitting reaction, this suggests that the temperature-promoted effect on water splitting may saturate at relatively low temperatures. In the in-situ FTIR spectra for dark (Fig. 4c) and light (Fig. 4d) reactions, no significant changes were observed within the 5–30 min timescale, likely due to the fast reaction rate at 500 °C reaching equilibrium within 5 min. However, there are notable differences between the light and dark conditions. For water molecule-related groups, no significant differences were observed, while hydroxyl-related groups showed distinct differences. The M−OH group is more prominent under light conditions compared to dark conditions, whereas the O-H group is more pronounced in the dark than under light. This could be attributed to different reaction pathways: dark reactions rely on thermochemical water splitting involving surface oxygen vacancies, while light reactions primarily involve photocatalytic water adsorption directly on metal atoms without oxygen vacancies.

3.6. Proposed mechanism of SOPC

Solid Oxide Photoelectrolysis Cells (SOPCs) utilize the photothermal-electric synergistic effects to split water for hydrogen production. This study focuses on the generation of photocurrent and its underlying mechanisms (Fig. 5). At high temperatures (~800 °C), the 8ALST photoresponsive electrode becomes rich in oxygen vacancies (O_V) and exhibits significant intra-bandgap states caused by defects, leading to notable visible-light absorption up to 800 nm. An electrical bias of 0.8–2.0 V accelerates carrier transport, mitigating the recombination of photogenerated carriers caused by bulk defects and high temperatures, resulting in a remarkable external quantum efficiency (EQE) of 30.2 %. Illumination alters surface reaction characteristics by introducing new water-splitting reaction sites that are independent of surface oxygen vacancies, significantly enhancing hydrogen evolution reaction (HER) activity. The optical mechanism can be divided into three temporal phases: less than 10 s, 10–600 s, and more than 600 s. Within the first 10 s, the photoresponse is dominated by photocatalysis, where photogenerated carriers in 8ALST reduce the charge transfer resistance during HER, producing the majority (>50 %) of the photocurrent. Between 10 and 600 s, the photoresponse is governed by photoelectrochemical reactions. Photoreactions on the 8ALST surface create additional oxygen vacancies, which, in turn, increase bulk oxygen vacancies, enhancing overall cell performance and generating the remaining photocurrent. Beyond 600 s, the photoresponse is dominated by the Light Healing Effect (LHE), where photo-induced oxygen vacancies slow down the accumulation of oxygen ions over time, suppressing interfacial oxygen accumulation and secondary phase formation, thereby mitigating cell degradation. Moreover, this effect continues to enhance cell performance over long timescales, lasting at least 40 h.

4. Conclusion

This study reports the first observation of significant photocurrent generation in a Solid Oxide Photoelectrolysis Cell (SOPC) device employing various aluminum-doped $SrTiO_3$ (ALST) photoresponsive electrodes based on ALST/YSZ/YSZ-LSM cells. Experimental results demonstrated that 8ALST, prepared using the melting method, exhibited superior optical and photocatalytic performance. An optimal photocurrent of 56.89 mA/cm^2 (equivalent to 10.62 mol/m^2/h of hydrogen production with an EQE of 30.2 %) was observed at 850 °C, 2.0 V, and 50 % H_2O + 50 % H_2. An optimal percentage photocurrent of 21.39 % (compared to dark current) was observed at 800 °C, 0.8 V, and 50 % H_2O + 0 % H_2. Based on the percentage photocurrent, the 8ALST photoresponsive electrode showed significant effectiveness at potentials above the water-splitting threshold (≥ 0.8 V). It was highly responsive to temperature changes, with a 50 °C variation leading to a 105.5 % difference in photocurrent. The presence of hydrogen in the atmosphere enhanced electrochemical performance, while higher water content improved optical performance.

In further SOPC experiments, the relatively stable cell temperature indicated that photocatalysis and photoelectrochemical reactions, rather than photothermal effects, primarily drove the photocurrent. During light/dark Electrochemical Impedance Spectroscopy (EIS), changes in high-frequency impedance accounted for 63.7 % of the total impedance change. In time–frequency analysis, most of the

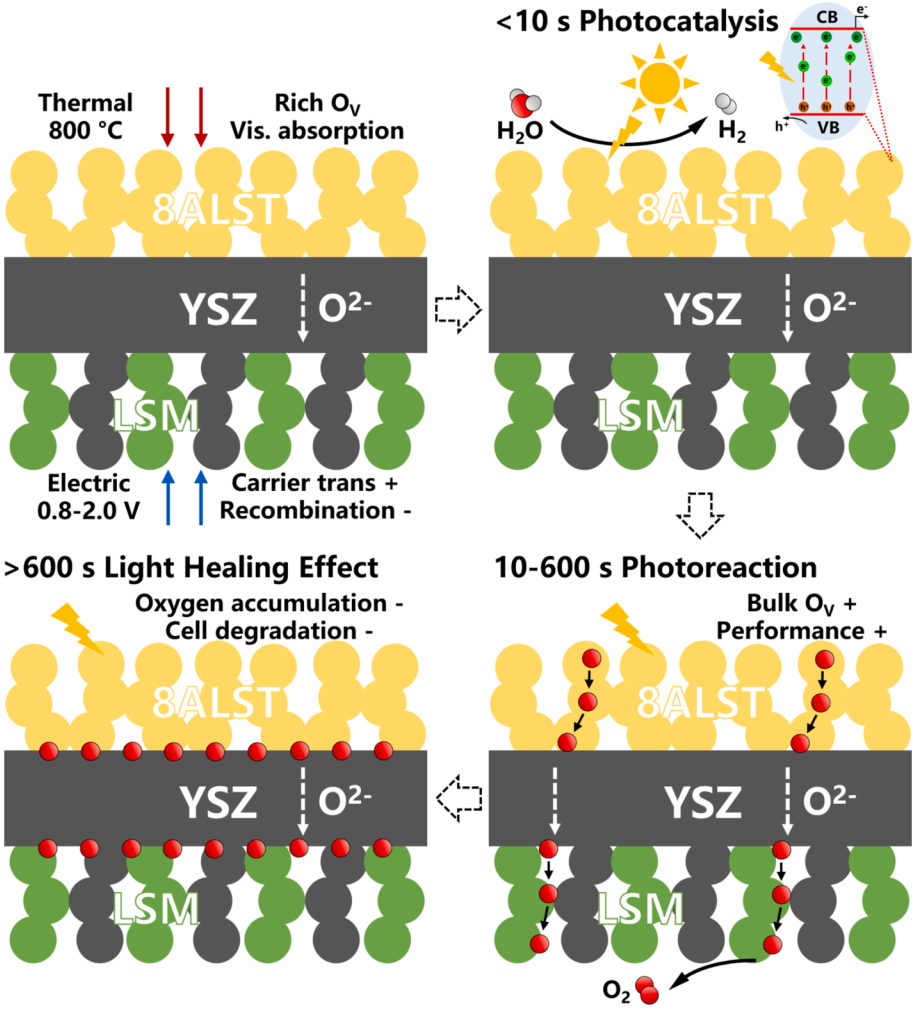

Fig. 5. Mechanism diagram of Solid Oxide Photoelectrolysis Cell (SOPC).

photocurrent was generated within 10 s of illumination, indicating that changes in charge transfer impedance due to photogenerated carriers (photocatalysis) played the primary role, while photoelectrochemical reactions were secondary. Additionally, the Light Healing Effect (LHE), driven by photo-induced oxygen vacancies, significantly mitigated cell degradation, extending the cell's lifespan by up to 3.59 times. At the material level, aluminum doping via the melting method resulted in a more regular cubic morphology, increased bulk oxygen vacancies, and reduced Ti^{3+} recombination centers, collectively suppressing photogenerated carrier recombination and enhancing optical performance. In contrast, aluminum doping via the sol–gel method and the strategy of optical-electrical functional separation did not achieve the same enhancement in optical performance compared to LST. As a semiconductor primarily absorbing ultraviolet light at room temperature, 8ALST exhibited significant visible-light absorption above 250 °C and generated notable visible-light photocurrent (> 400 nm) in SOPC applications. At 800 °C, the Incident Photon-to-Current Efficiency (IPCE) ranged from 19.3 % to 5.4 % in the 350–800 nm wavelength range, with a significant decline in visible-light absorption upon cooling. This expanded absorption range and temperature-dependent optical behavior highlight 8ALST's potential to optimize solar energy utilization in SOPCs, making it a versatile material for solar-driven hydrogen production under varying operational conditions.

CRediT authorship contribution statement

Guangyu Deng: Writing – review & editing, Writing – original draft, Visualization, Validation, Software, Resources, Methodology, Investigation, Formal analysis, Data curation, Conceptualization. **Chenyu Xu:** Writing – review & editing, Supervision, Project administration, Funding acquisition, Formal analysis. **Jinhao Mei:** Validation, Methodology, Investigation, Conceptualization. **Chen-Ge Chen:** Methodology, Investigation. **Yanwei Zhang:** Supervision, Project administration, Funding acquisition.

Declaration of competing interest

The authors declare that they have no known competing financial interests or personal relationships that could have appeared to influence the work reported in this paper.

Acknowledgements

This work is supported by the National Natural Science Foundation of China (52341602), the National Key Research and Development Project (2023YFC3710800), the Zhejiang Provincial Natural Science Foundation of China under Grant (LQ24E060001), the Zhejiang Provincial Natural Science Foundation of China under Grant (LDT23E06014E06), the Fundamental Research Funds for the Central Universities (2022ZFJH04) and the Scientific Research Fund of Zhejiang University (XY2023037).

Author contributions

G. D. designed and conducted the experiments, analyzed the data and wrote the manuscript; J. M. conducted cell preparations and a part of SOPC tests; C. C. performed a part of photoresponsive electrode synthesis; C. X. and Y. Z. received the funding for the projects and supervised the whole project.

Appendix A. Supplementary data

Supplementary data to this article can be found online at https://doi.org/10.1016/j.cej.2024.158794.

Data availability

Data will be made available on request.

References

[1] A. Hauch, R. Küngas, P. Blennow, A.B. Hansen, J.B. Hansen, B.V. Mathiesen, M.B. Mogensen, Recent advances in solid oxide cell technology for electrolysis, Science 370 (2020) eaba6118. doi: 10.1126/science.aba6118.

[2] Y. Zhao, Z. Niu, J. Zhao, L. Xue, X. Fu, J. Long, Recent Advancements in Photoelectrochemical Water Splitting for Hydrogen Production, Electrochem. Energy Rev. 6 (2023) 14, https://doi.org/10.1007/s41918-022-00153-7.

[3] A.Q. Al-Shetwi, Sustainable development of renewable energy integrated power sector: Trends, environmental impacts, and recent challenges, Sci. Total Environ. 822 (2022) 153645, https://doi.org/10.1016/j.scitotenv.2022.153645.

[4] X.-W. Lv, W.-W. Tian, Z.-Y. Yuan, Recent Advances in High-Efficiency Electrocatalytic Water Splitting Systems, Electrochem. Energy Rev. 6 (2023) 23, https://doi.org/10.1007/s41918-022-00159-1.

[5] A. Kovac, M. Paranos, D. Marcius, Hydrogen in energy transition: A review, Int. J. Hydrogen Energy 46 (2021) 10016–10035, https://doi.org/10.1016/j.ijhydene.2020.11.256.

[6] P.J. Megía, A.J. Vizcaíno, J.A. Calles, A. Carrero, Hydrogen Production Technologies: From Fossil Fuels toward Renewable Sources, A Mini Review, Energy Fuels 35 (2021) 16403–16415, https://doi.org/10.1021/acs.energyfuels.1c02501.

[7] M. Nasser, T.F. Megahed, S. Ookawara, H. Hassan, A review of water electrolysis–based systems for hydrogen production using hybrid/solar/wind energy systems, Environ Sci Pollut Res 29 (2022) 86994–87018, https://doi.org/10.1007/s11356-022-23323-y.

[8] H. Shimada, T. Yamaguchi, H. Kishimoto, H. Sumi, Y. Yamaguchi, K. Nomura, Y. Fujishiro, Nanocomposite electrodes for high current density over 3 A cm−2 in solid oxide electrolysis cells, Nat Commun 10 (2019) 5432, https://doi.org/10.1038/s41467-019-13426-5.

[9] C. Duan, R. Kee, H. Zhu, N. Sullivan, L. Zhu, L. Bian, D. Jennings, R. O'Hayre, Highly efficient reversible protonic ceramic electrochemical cells for power generation and fuel production, Nat Energy 4 (2019) 230–240, https://doi.org/10.1038/s41560-019-0333-2.

[10] D. Ferrero, A. Lanzini, M. Santarelli, P. Leone, A comparative assessment on hydrogen production from low- and high-temperature electrolysis, Int. J. Hydrogen Energy 38 (2013) 3523–3536, https://doi.org/10.1016/j.ijhydene.2013.01.065.

[11] Y. Cao, T. Parikhani, A solar-driven lumped SOFC/SOEC system for electricity and hydrogen production: 3E analyses and a comparison of different multi-objective optimization algorithms, J. Clean. Prod. 271 (2020) 122457, https://doi.org/10.1016/j.jclepro.2020.122457.

[12] H. Song, S. Luo, H. Huang, B. Deng, J. Ye, Solar-Driven Hydrogen Production: Recent Advances, Challenges, and Future Perspectives, ACS Energy Lett. 7 (2022) 1043–1065, https://doi.org/10.1021/acsenergylett.1c02591.

[13] Q. Zhang, Z. Chang, M. Fu, F. Nie, T. Ren, X. Li, Thermal performance analysis of an integrated solar reactor using solid oxide electrolysis cells (SOEC) for hydrogen production, Energ. Conver. Manage. 264 (2022) 115762, https://doi.org/10.1016/j.enconman.2022.115762.

[14] M.S. Khan, Z. Lin, L. Lin, M. Abid, H.M. Ali, C. Chen, Techno-economic analysis of solar-driven co-electrolysis for renewable methanol production using SOEC, Energ. Conver. Manage. 302 (2024) 118129, https://doi.org/10.1016/j.enconman.2024.118129.

[15] J. Immonen, K.M. Powell, Hydrogen from solar? A Rigorous Analysis of Solar Energy Integration Concepts for a High Temperature Steam Electrolysis Plant, Energy Conversion and Management 298 (2023) 117759 https://doi.org/10.1016/j.enconman.2023.117759.

[16] F. Wang, L. Wang, Y. Ou, X. Lei, J. Yuan, X. Liu, Y. Zhu, Thermodynamic analysis of solid oxide electrolyzer integration with engine waste heat recovery for hydrogen production, Case Stud. Therm. Eng. 27 (2021) 101240, https://doi.org/10.1016/j.csite.2021.101240.

[17] M. Lin, S. Haussener, An integrated concentrated solar fuel generator utilizing a tubular solid oxide electrolysis cell as solar absorber, J. Power Sources 400 (2018) 592–604, https://doi.org/10.1016/j.jpowsour.2018.08.009.

[18] H. Jiang, X. Liu, D. Wang, Z. Qiao, D. Wang, F. Huang, H. Peng, C. Hu, Designing high-efficiency light-to-thermal conversion materials for solar desalination and photothermal catalysis, Journal of Energy, Chemistry 79 (2023) 581–600, https://doi.org/10.1016/j.jechem.2023.01.009.

[19] M. Mehrpooya, M. Karimi, Hydrogen production using solid oxide electrolyzer integrated with linear Fresnel collector, Rankine Cycle and Thermochemical Energy Storage Tank, Energy Conversion and Management 224 (2020) 113359, https://doi.org/10.1016/j.enconman.2020.113359.

[20] W. Wang, Y. Sun, H.S. Majdi, A. Deifalla, T.R. Alsenani, Z. Zhao, Z. Su, W. Zhang, M.A.H. Abdelmohimen, Multi-aspect investigation and multi-criteria optimization of a novel solar-geothermal-based polygeneration system using flat plate and concentrated photovoltaic thermal solar collectors, Process Saf. Environ. Prot. 174 (2023) 485–509, https://doi.org/10.1016/j.psep.2023.03.023.

[21] X. Yang, D. Wang, Photocatalysis: From Fundamental Principles to Materials and Applications, ACS Appl. Energy Mater. 1 (2018) 6657–6693, https://doi.org/10.1021/acsaem.8b01345.

[22] X. Song, G. Wei, J. Sun, C. Peng, J. Yin, X. Zhang, Y. Jiang, H. Fei, Overall photocatalytic water splitting by an organolead iodide crystalline material, Nat Catal 3 (2020) 1027–1033, https://doi.org/10.1038/s41929-020-00543-4.

[23] M. Kumar, B. Meena, P. Subramanyam, D. Suryakala, C. Subrahmanyam, Recent trends in photoelectrochemical water splitting: the role of cocatalysts, NPG Asia Mater 14 (2022) 1–21, https://doi.org/10.1038/s41427-022-00436-x.

[24] J.P. Barham, B. König, Synthetic Photoelectrochemistry, Angew. Chem. Int. Ed. 59 (2020) 11732–11747, https://doi.org/10.1002/anie.201913767.

[25] M.Z. Rahman, T. Edvinsson, J. Gascon, Hole utilization in solar hydrogen production, Nat Rev Chem 6 (2022) 243–258, https://doi.org/10.1038/s41570-022-00366-w.

[26] F. Li, L. Cheng, J. Fan, Q. Xiang, Steering the behavior of photogenerated carriers in semiconductor photocatalysts: a new insight and perspective, J. Mater. Chem. A 9 (2021) 23765–23782, https://doi.org/10.1039/D1TA06899G.

[27] D. Chen, Y. Cheng, N. Zhou, P. Chen, Y. Wang, K. Li, S. Huo, P. Cheng, P. Peng, R. Zhang, L. Wang, H. Liu, Y. Liu, R. Ruan, Photocatalytic degradation of organic pollutants using TiO2-based photocatalysts: A review, J. Clean. Prod. 268 (2020) 121725, https://doi.org/10.1016/j.jclepro.2020.121725.

[28] S. Nishioka, F.E. Osterloh, X. Wang, T.E. Mallouk, K. Maeda, Photocatalytic water splitting, Nat Rev Methods Primers 3 (2023) 1–15, https://doi.org/10.1038/s43586-023-00226-x.

[29] S. Fang, M. Rahaman, J. Bharti, E. Reisner, M. Robert, G.A. Ozin, Y.H. Hu, Photocatalytic CO2 reduction, Nat Rev Methods Primers 3 (2023) 1–21, https://doi.org/10.1038/s43586-023-00243-w.

[30] T. Li, M. Wu, S. Wu, S. Xiang, J. Xu, J. Chao, T. Yan, T. Deng, R. Wang, Highly conductive phase change composites enabled by vertically-aligned reticulated graphite nanoplatelets for high-temperature solar photo/electro-thermal energy conversion, harvesting and storage, Nano Energy (2021).

[31] S. Limsakul, C. Thanachayanont, A. Siyasukh, M. Jaideekard, S. Yimklan, P. Kijjanapanich, Y. Chimupala, High efficiency azo dye removal via a combination of adsorption and photocatalytic processes using heterojunction Titanium dioxide nanoparticles on hierarchical porous carbon, Environ. Res. 260 (2024) 119627, https://doi.org/10.1016/j.envres.2024.119627.

[32] B. Moss, Q. Wang, K.T. Butler, R. Grau-Crespo, S. Selim, A. Regoutz, T. Hisatomi, R. Godin, D.J. Payne, A. Kafizas, K. Domen, L. Steier, J.R. Durrant, Linking in situ charge accumulation to electronic structure in doped SrTiO3 reveals design principles for hydrogen-evolving photocatalysts, Nat. Mater. 20 (2021) 511–517, https://doi.org/10.1038/s41563-020-00868-2.

[33] T. Takata, J. Jiang, Y. Sakata, M. Nakabayashi, N. Shibata, V. Nandal, K. Seki, T. Hisatomi, K. Domen, Photocatalytic water splitting with a quantum efficiency of almost unity, Nature 581 (2020) 411–414, https://doi.org/10.1038/s41586-020-2278-9.

[34] R. Li, T. Takata, B. Zhang, C. Feng, Q. Wu, C. Cui, Z. Zhang, K. Domen, Y. Li, Criteria for Efficient Photocatalytic Water Splitting Revealed by Studying Carrier Dynamics in a Model Al-doped SrTiO3 Photocatalyst, Angew. Chem. 135 (2023) e202313537.

[35] X. Zhou, N. Yan, K.T. Chuang, J. Luo, Progress in La-doped SrTiO 3 (LST)-based anode materials for solid oxide fuel cells, RSC Adv. 4 (2014) 118–131, https://doi.org/10.1039/C3RA42666A.

[36] X. Yang, K. Sun, M. Ma, C. Xu, R. Ren, J. Qiao, Z. Wang, S. Zhen, R. Hou, W. Sun, Achieving strong chemical adsorption ability for efficient carbon dioxide electrolysis, Appl Catal B 272 (2020) 118968, https://doi.org/10.1016/j.apcatb.2020.118968.

[37] D. Navas, S. Fuentes, A. Castro-Alvarez, E. Chavez-Angel, Review on Sol-Gel Synthesis of Perovskite and Oxide Nanomaterials, Gels 7 (2021) 275, https://doi.org/10.3390/gels7040275.

[38] Y.-G. Lee, Y.-C. Cheng, Y.-T. Lin, J.C.S. Wu, W.-Y. Yu, M.M. Kržmanc, S. Gupta, E. Kotomin, Photocatalytic Water Splitting of Al-Doped RhxCr2–xO3/SrTiO3 Synthesized by Flux Method: Elucidating the Role of Different Molten Salts, J. Phys. Chem. C 127 (2023) 9981–9991, https://doi.org/10.1021/acs.jpcc.3c00483.

[39] M. Ni, M.K.H. Leung, D.Y.C. Leung, Technological development of hydrogen production by solid oxide electrolyzer cell (SOEC), Int. J. Hydrogen Energy 33 (2008) 2337–2354, https://doi.org/10.1016/j.ijhydene.2008.02.048.

[40] G. Deng, J. Mei, Y. Xie, J. Han, M. Wang, C. Xu, Y. Zhang, Photoinduced Mitigation of Solid Oxide Electrolysis Cell Degradation: Light Healing Effect on Oxygen Vacancies, ACS Appl. Energy Mater. 7 (2024) 373–379, https://doi.org/10.1021/acsaem.3c02754.

[41] C.J. Howard, G.R. Lumpkin, R.I. Smith, Z. Zhang, Crystal structures and phase transition in the system SrTiO3–La2/3TiO3, J. Solid State Chem. 177 (2004) 2726–2732, https://doi.org/10.1016/j.jssc.2004.04.018.

[42] P. Makuła, M. Pacia, W. Macyk, How To Correctly Determine the Band Gap Energy of Modified Semiconductor Photocatalysts Based on UV–Vis Spectra, J. Phys. Chem. Lett. 9 (2018) 6814–6817, https://doi.org/10.1021/acs.jpclett.8b02892.
[43] K. Sivula, Mott–Schottky Analysis of Photoelectrodes: Sanity Checks Are Needed, ACS Energy Lett. 6 (2021) 2549–2551, https://doi.org/10.1021/acsenergylett.1c01245.
[44] X. Zhang, Z. Li, T. Liu, M. Li, C. Zeng, H. Matsumoto, H. Han, Water oxidation sites located at the interface of Pt/SrTiO3 for photocatalytic overall water splitting, Chin. J. Catal. 43 (2022) 2223–2230, https://doi.org/10.1016/S1872-2067(21)64048-2.
[45] R. Djellabi, M.F. Ordonez, F. Conte, E. Falletta, C.L. Bianchi, I. Rossetti, A review of advances in multifunctional XTiO3 perovskite-type oxides as piezo-photocatalysts for environmental remediation and energy production, J. Hazard. Mater. 421 (2022) 126792, https://doi.org/10.1016/j.jhazmat.2021.126792.
[46] Y. Luo, W. Li, Y. Shi, Y. Wang, N. Cai, Reversible H2/H2O electrochemical conversion mechanisms on the patterned nickel electrodes, Int. J. Hydrogen Energy 42 (2017) 25130–25142, https://doi.org/10.1016/j.ijhydene.2017.08.138.
[47] Z. Du, K. Xu, F. Zhu, Y. Xu, F. He, H. Gao, W. Gong, Y. Choi, Y. Chen, Indium-Doping-Induced Nanocomposites with Improved Oxygen Reaction Activity and Durability for Reversible Protonic Ceramic Electrochemical Cell Air Electrodes, Adv. Funct. Mater. (2024) 2409188, https://doi.org/10.1002/adfm.202409188.
[48] K. Chen, Q. Weng, Z. Yue, J. Huang, J. Qian, Z. Chen, L. Zhang, C. Guan, S.P. Jiang, N. Ai, Surface Chemistry Modulation of BaGd0.8La0.2Co2O6−δ As Active Air Electrode for Solid Oxide Cells, ACS Appl, Mater. Interfaces 16 (2024) 31181–31190, https://doi.org/10.1021/acsami.4c05162.
[49] L. Hou, M. Zhang, Z. Guan, Q. Li, J. Yang, Effect of annealing ambience on the formation of surface/bulk oxygen vacancies in TiO2 for photocatalytic hydrogen evolution, Appl. Surf. Sci. 428 (2018) 640–647, https://doi.org/10.1016/j.apsusc.2017.09.144.
[50] T. Yamamoto, R. Palani, H. Kitami, H. Makino, Free-carrier localization and electron–phonon interaction in transparent conductive oxide films, JSAP Review 2024 (2024), https://doi.org/10.11470/jsaprev.240404.
[51] L.-L. Tan, W.-J. Ong, S.-P. Chai, A.R. Mohamed, Photocatalytic reduction of CO2 with H2O over graphene oxide-supported oxygen-rich TiO2 hybrid photocatalyst under visible light irradiation: Process and kinetic studies, Chem. Eng. J. 308 (2017) 248–255, https://doi.org/10.1016/j.cej.2016.09.050.
[52] O.A. Marina, N.L. Canfield, J.W. Stevenson, Thermal, electrical, and electrocatalytical properties of lanthanum-doped strontium titanate, Solid State Ion. 149 (2002) 21–28, https://doi.org/10.1016/S0167-2738(02)00140-6.
[53] K. Uematsu, O. Sakurai, N. Mizutani, M. Kato, Electrical properties of La-doped SrTiO3 (La: 0.1 to 2.0 at %) single crystals grown by xenon-arc image floating zone method, J Mater Sci 19 (1984) 3671–3679, https://doi.org/10.1007/BF02396939.
[54] A.Y. Ahmed, T.A. Kandiel, I. Ivanova, D. Bahnemann, Photocatalytic and photoelectrochemical oxidation mechanisms of methanol on TiO2 in aqueous solution, Appl. Surf. Sci. 319 (2014) 44–49, https://doi.org/10.1016/j.apsusc.2014.07.134.
[55] J.B. Sambur, P. Chen, Distinguishing Direct and Indirect Photoelectrocatalytic Oxidation Mechanisms Using Quantitative Single-Molecule Reaction Imaging and Photocurrent Measurements, J. Phys. Chem. C 120 (2016) 20668–20676, https://doi.org/10.1021/acs.jpcc.6b01848.
[56] Y. Wang, W. Li, L. Ma, W. Li, X. Liu, Degradation of solid oxide electrolysis cells: Phenomena, mechanisms, and emerging mitigation strategies—A review, J. Mater. Sci. Technol. 55 (2020) 35–55, https://doi.org/10.1016/j.jmst.2019.07.026.
[57] M. Reisert, A. Aphale, P. Singh, Solid Oxide Electrochemical Systems: Material Degradation Processes and Novel Mitigation Approaches, Materials 11 (2018) 2169, https://doi.org/10.3390/ma11112169.
[58] J. Dhanalakshmi, S. Iyyapushpam, S.T. Nishanthi, M. Malligavathy, D.P. Padiyan, Investigation of oxygen vacancies in Ce coupled TiO2 nanocomposites by Raman and PL spectra, Adv. Nat. Sci: Nanosci. Nanotechnol. 8 (2017) 015015, https://doi.org/10.1088/2043-6254/aa5984.
[59] H. Trabelsi, M. Bejar, E. Dhahri, M.P.F. Graça, M.A. Valente, M.J. Soares, N. A. Sobolev, Raman, EPR and ethanol sensing properties of oxygen-Vacancies SrTiO3-δ compounds, Appl. Surf. Sci. 426 (2017) 386–390, https://doi.org/10.1016/j.apsusc.2017.07.128.
[60] H. Tan, Z. Zhao, W. Zhu, E.N. Coker, B. Li, M. Zheng, W. Yu, H. Fan, Z. Sun, Oxygen Vacancy Enhanced Photocatalytic Activity of Pervoskite SrTiO3, ACS Appl. Mater. Interfaces 6 (2014) 19184–19190, https://doi.org/10.1021/am5051907.
[61] S. Tougaard, Energy loss in XPS: Fundamental processes and applications for quantification, non-destructive depth profiling and 3D imaging, J. Electron Spectrosc. Relat. Phenom. 178–179 (2010) 128–153, https://doi.org/10.1016/j.elspec.2009.08.005.
[62] D.B. Drasbæk, P. Blennow, T. Heiredal-Clausen, J. Rass-Hansen, G. Perin, J.V. T. Høgh, A. Hauch, Exploring electrochemical impedance spectroscopy to identify and quantify degradation in commercial solid oxide electrolysis stacks, Fuel Cells 23 (2023) 454–462, https://doi.org/10.1002/fuce.202300023.
[63] E.-C. Shin, P.-A. Ahn, H.-H. Seo, J.-M. Jo, S.-D. Kim, S.-K. Woo, J.H. Yu, J. Mizusaki, J.-S. Lee, Polarization mechanism of high temperature electrolysis in a Ni–YSZ/YSZ/LSM solid oxide cell by parametric impedance analysis, Solid State Ion. 232 (2013) 80–96, https://doi.org/10.1016/j.ssi.2012.10.028.
[64] Y. Yan, Q. Fang, L. Blum, W. Lehnert, Performance and degradation of an SOEC stack with different cell components, Electrochim. Acta 258 (2017) 1254–1261, https://doi.org/10.1016/j.electacta.2017.11.180.
[65] W. Pan, K. Chen, N. Ai, Z. Lü, S.P. Jiang, Mechanism and Kinetics of Ni-Y2O3-ZrO2 Hydrogen Electrode for Water Electrolysis Reactions in Solid Oxide Electrolysis Cells, J. Electrochem. Soc. 163 (2015) F106, https://doi.org/10.1149/2.0801602jes.
[66] K.L.A. Chan, S.G. Kazarian, Attenuated total reflection Fourier-transform infrared (ATR-FTIR) imaging of tissues and live cells, Chem. Soc. Rev. 45 (2016) 1850–1864, https://doi.org/10.1039/C5CS00515A.
[67] H. Kaur, B. Rana, D. Tomar, S. Kaur, K.C. Jena, Fundamentals of ATR-FTIR Spectroscopy and Its Role for Probing In-Situ Molecular-Level Interactions, in: D.K. Singh, M. Pradhan, A. Materny (Eds.), Modern Techniques of Spectroscopy: Basics, Instrumentation, and Applications, Springer, Singapore, 2021: pp. 3–37. doi: 10.1007/978-981-33-6084-6_1.